

Article

# Linear and Non-Linear Trends for Seasonal NO<sub>2</sub> and SO<sub>2</sub> Concentrations in the Southern Hemisphere (2004–2016)

Adrián Yuchechechén<sup>1,\*</sup> , Susan Gabriela Lakkis<sup>2,3</sup> and Pablo Canziani<sup>1</sup>

<sup>1</sup> Universidad Tecnológica Nacional (UTN), Facultad Regional Buenos Aires (FRBA), Consejo Nacional de Investigaciones Científicas y Técnicas (CONICET), Unidad de Investigación y Desarrollo de las Ingenierías (UIDI), Buenos Aires C1407IVT, Argentina; pocanziani@frba.utn.edu.ar

<sup>2</sup> Pontificia Universidad Católica Argentina, Facultad de Ingeniería y Ciencias Agrarias, Buenos Aires C1107AAZ, Argentina; gabyLakkis@uca.edu.ar

<sup>3</sup> UTN, FRBA, UIDI, Buenos Aires C1407IVT, Argentina

\* Correspondence: aeyuchechech@frba.utn.edu.ar; Tel.: +54-11-4567-7268

Received: 30 June 2017; Accepted: 24 August 2017; Published: 28 August 2017

**Abstract:** In order to address the behaviour of nitrogen dioxide (NO<sub>2</sub>) and sulphur dioxide (SO<sub>2</sub>) in the context of a changing climate, linear and non-linear trends for the concentrations of these two trace gases were estimated over their seasonal standardised variables in the Southern Hemisphere—between the Equator and 60° S—using data retrieved by the Ozone Monitoring Instrument, for the period 2004–2016. A rescaling was applied to the calculated linear trends so that they are expressed in Dobson units (DU) per decade. Separately, the existence of monotonic—not necessarily linear—trends was addressed by means of the Mann-Kendall test. Results indicate that the SO<sub>2</sub> exhibits significant linear trends in the planetary boundary layer only; they are present in all the analysed seasons but just in a small number of grid cells that are generally located over the landmasses or close to them. The SO<sub>2</sub> concentrations in the quarterly time series exhibit, on average, a linear trend that is just below 0.08 DU decade<sup>−1</sup> when significant and not significant values are considered altogether, but this figure increases to 0.80 DU decade<sup>−1</sup> when only the significant trends are included. On the other hand, an important number of pixels in the lower troposphere, the middle troposphere, and the lower stratosphere have significant monotonic upward or downward trends. As for the NO<sub>2</sub>, no significant linear trends were found either in the troposphere or in the stratosphere, yet monotonic upward and downward trends were observed in the former and latter layers, respectively. Unlike the linear trends, semi-linear and non-linear trends were seen over the continents and in remote regions over the oceans. This suggests that pollutants are transported away from their sources by large-scale circulation and redistributed hemispherically. The combination of regional meteorological phenomena with atmospheric chemistry was raised as a possible explanation for the observed trends. If extrapolated, these trends are in an overall contradiction with the projected emissions of both gases for the current century.

**Keywords:** nitrogen dioxide; sulphur dioxide; concentrations; linear trends; non-linear trends; Mann-Kendall test; Southern Hemisphere

## 1. Introduction

There is now widespread consensus that changes in the composition of the Earth's atmosphere caused by human activities play a relevant role in the Earth's climate system. Unlike the greenhouse gases that induce a positive radiative forcing, aerosol particles influence the global radiation budget causing a net negative radiative forcing associated with a cooling effect on the atmosphere ([1] and

references therein). Broadly speaking, the radiative contribution of the aerosols can be centred in three main categories depending on what they interact with: aerosols-surface, aerosols-radiation and aerosols-clouds, or considering the aerosols' influence on the atmosphere as a direct, indirect, or semi-direct effect [2–5]. In addition to the radiative influence, aerosols are significant contributors to air pollution and they have a direct linkage with the biogeochemical cycles of the atmosphere, the oceans and the surfaces, acting as micronutrients for the marine and terrestrial biosphere. Aerosol deposition can also have detrimental environmental effects (e.g., the acidification of precipitation by sulphurs [6]) with impacts on the aquatic and terrestrial ecosystems [7–9], yet the benefits or the detrimental effects on ecological processes depend upon both the amount and composition of deposition and the underlying ecosystem conditions.

Amidst the aerosols with greater relevance, nitrogen dioxide (NO<sub>2</sub>) and sulphur dioxide (SO<sub>2</sub>) must be considered since they are reactive short-lived atmospheric trace gases, with both anthropogenic and natural sources that strongly impact on human health and the environmental degradation either directly or through the formation of secondary aerosols [10,11]. The main sources of nitrogen oxide compounds, nitric oxide (NO) and NO<sub>2</sub>—collectively referred to as NO<sub>x</sub>—include fuel combustion, biomass burning, soil emissions and lightning, and they can impact on climate in a number of interconnected ways [12]. Tropospheric NO<sub>2</sub> is a highly reactive and toxic gas which, in the presence of sunlight, water vapour (H<sub>2</sub>O) and carbon monoxide (CO) or volatile organic compounds, drives the production of ozone (O<sub>3</sub>) and hydroxyl radicals (OH), the principal tropospheric oxidants [12,13]. In the stratosphere, NO<sub>x</sub> contributes to the ozone-loss cycles [14] and may indicate long-term changes in the tropospheric emissions of the long-lived nitrous oxide (N<sub>2</sub>O) [13]. On the other hand, SO<sub>2</sub> is a colourless, non-flammable, non-explosive gas, toxic at high concentrations, and its principal contribution to air pollution is related to the acidification of precipitation and subsequent impacts on the receiving ecosystems [6].

SO<sub>2</sub> dissolves in cloud droplets and oxidises to form sulphuric acid (H<sub>2</sub>SO<sub>4</sub>) [15], which can fall to the Earth as acid rain or snow, or form sulphate aerosol particles in the atmosphere through oxidation [11]. The main contributions of SO<sub>2</sub> are related to anthropogenic emissions (including the combustion of sulphur-containing fuels [15]) and natural phenomena (including biomass burning [16]) and the oxidation of dimethyl sulphide (CH<sub>3</sub>SCH<sub>3</sub>), emitted from phytoplankton [15], and from the degassing and eruptions of volcanoes [16]. During long-term persistent volcanic eruptions SO<sub>2</sub> can be injected into the stratosphere and converted to sulphate aerosols, reflecting the sunlight and therefore inducing a cooling effect on the Earth's climate. They also have a role in ozone depletion. Volcanic SO<sub>2</sub> is often injected into the atmosphere at altitudes above the planetary boundary layer (PBL), while anthropogenic SO<sub>2</sub> emissions are predominantly in or just above the PBL [11]. Additionally, SO<sub>2</sub> in the atmosphere is associated with adverse health effects, including respiratory and cardiovascular diseases. The United States Environmental Protection Agency (EPA) has estimated that two thirds of SO<sub>2</sub> and a fourth of NO<sub>x</sub> found in the atmosphere come from the burning of fossil fuels to generate electricity [17]. World Health Organization guidelines recommended daily SO<sub>2</sub> exposure levels not to exceed 125 µg m<sup>-3</sup> on average over a 24 h period [18]. NO<sub>2</sub>, SO<sub>2</sub>, and their oxidised products O<sub>3</sub> and PM<sub>2.5</sub> (particulate matter with aerodynamic diameter less than 2.5 µm) are designated as “criteria pollutants” by both the European Commission and the EPA (see e.g., [11] and references therein). PM<sub>2.5</sub> have serious health effects, and it also causes acidification of water and the biosphere, with adverse consequences on plants, soils, and weather and climate through direct radiative forcing and indirect modification of cloud formation and optical properties ([11] and references therein).

The preceding lines highlighted the importance of assessing the role of aerosols and their impacts on the Earth's climate system, for which a global understanding of their spatial and temporal behaviour is required. Reliable, up-to-date inventories of emissions and concentrations are the first step when attempting to evaluate these impacts and to address the effects on the climate system over different timescales. Although in situ measurements provide valuable information, they are insufficient to these particular aims for they are scarce spatially, temporally, or both and they must be at least

complemented by remotely-sensed data. Following this, the Ozone Monitoring Instrument (OMI) provides the scientific community with a valuable source of information since it is the first space-borne hyperspectral ultraviolet/visible spectrometer that enables a continuous mapping of several trace gases and ozone, including SO<sub>2</sub> and NO<sub>2</sub>, globally and on a daily basis [19]. There have been an increasing number of studies related to NO<sub>x</sub> and SO<sub>x</sub> emissions in the last decade [10,13,20–25]. However, few of them were devoted to analysing linear and non-linear trends in the Southern Hemisphere (SH), and those papers dealing with this particular topic only studied specific locations [26]. In order to fill this gap and to complement the existing studies, this paper presents a comprehensive analysis of NO<sub>2</sub> and SO<sub>2</sub> linear and non-linear trends in the entire SH within the 2004–2016 period using OMI data.

## 2. Materials and Methods

The NO<sub>2</sub> and SO<sub>2</sub> data used in this research were retrieved by the OMI aboard the Aura spacecraft, which was launched in July 2004 [27,28]. The OMI is a nadir solar backscatter spectrometer that operates in the 270–500 nm spectral range [19]. It began collecting data in August 2004 [27], and data production commenced in October the same year [28]. OMI has the highest spatial resolution, the least degradation, and the longest record among all satellite ultraviolet-visible instruments, which permits an improved space-borne estimation of NO<sub>2</sub> and SO<sub>2</sub> emissions and the study of their temporal behaviours ([11] and references therein).

The datasets for the two gas species were obtained from the Goddard Earth Sciences Data and Information Services Center (GES DISC) through the National Aeronautics and Space Administration's (NASA) Mirador search engine (<https://mirador.gsfc.nasa.gov/>). The NO<sub>2</sub> daily product corresponds to the OMNO2G version 3 dataset, whose coverage has a resolution of 0.25° × 0.25° on a global basis [29]. NO<sub>2</sub> measurements made by the OMI are performed in the visible spectrum within the 402–465 nm range [30]. Each OMNO2G daily file includes pixel information regarding the column concentrations of this gas in the troposphere (Trop) and the stratosphere (Strat), as well as the total column. All these quantities are expressed in molecules cm<sup>-2</sup>. A single quality flag (QF) for these three concentrations and a number of ancillary variables are included too. Only those records with a value of "0" for this QF should be used [29]. In a first processing of each daily file only those registries fulfilling this condition were selected. Under these circumstances, negative concentrations, should there be any, were flagged as missing data. Simultaneously, the concentrations were converted to Dobson Units (DU) (1 DU = 2.69 × 10<sup>16</sup> molecules cm<sup>-2</sup> [31]). This was done for the sake of homogeneity since the SO<sub>2</sub> concentrations are given in DU (see below), and also because it is a much more familiar unit that has been traditionally used in research efforts mainly related to ozone [32–34], but also dealing with other atmospheric constituents [35].

On the other hand, the SO<sub>2</sub> daily product used here was the OMSO2G version 3 dataset. It has a resolution of 0.125° × 0.125° [36]. The OMSO2G daily files include the following concentration estimates for this gas: PBL, lower troposphere (TRL), middle troposphere (TRM), and upper troposphere and lower stratosphere (STL), the former two associated with anthropogenic activity and the latter two associated with volcanic activity [27]. SO<sub>2</sub> PBL concentrations are estimated using the Band Residual Difference Algorithm [37], whereas concentrations in the rest of the layers are estimated using the Linear Fit Algorithm [16]. Unlike the NO<sub>2</sub> dataset, all these quantities are directly expressed in DU. Another difference with the NO<sub>2</sub> dataset is that there is an individual QF for each concentration. As with the NO<sub>2</sub>, a first processing was carried out for SO<sub>2</sub> but considering each individual QF. In cases where negative concentrations fulfilled the QF condition the values were flagged as missing.

Apart from the fact that both datasets have a different spatial resolution the concentrations for these two species are provided in an irregular grid that varies from day to day. A regridding was therefore carried out in order to overcome these drawbacks. Data was mapped into a common grid having a resolution of 1° and 1.25° in latitude and longitude, respectively, for both constituents. This was done in order to match a standard grid of 180 × 288 pixels in which different Total Ozone Mapping Spectrometer (TOMS) products—ozone, reflectivity, etc.—were given (e.g., [38,39]). More

specifically, the regridding process assigned a daily mean value to the centre of each of the 51,840 possible boxes. This mean value was calculated over all the daily non-missing available data that fell within  $-89.5 + (i - 1) \pm 0.5$  for  $i = 1, 2, \dots, 180$  and  $-179.375 + 1.25(j - 1) \pm 0.625$  for  $j = 1, 2, \dots, 288$  (latitude and longitude, respectively, both expressed in degrees). The outcome of this regridding is the mapping of daily irregular NO<sub>2</sub> and SO<sub>2</sub> global fields into a common regular grid. They constitute the starting point of this research. The period of analysis is the 2004–2016 period.

Long-term seasonal means and standard deviations (SDs) were calculated at each of the pixels of the TOMS-like grid for southern summer, autumn, winter, and spring, including data from December, January and February (DJF), March, April and May (MAM), June, July and August (JJA), and September, October and November (SON), respectively. A minimum number of three values were required in order not to consider the seasonal mean at any pixel as missing. All the seasons were brought together in order to represent the quarterly (Q) cycle. The long-term means and SDs for this case were calculated too. The seasonal means and SDs show prominent, yet spurious, loci of maximum values for the SO<sub>2</sub> concentrations—but not for the NO<sub>2</sub> concentrations—in southern Brazil (BRA). As an example, Figure 1 shows the Q mean concentrations for both gases. The high prominent SO<sub>2</sub> concentrations in the specified region are attributed to the so-called South Atlantic Anomaly (SAA), a region centred in central South America (SA) where the intensity of the Earth’s magnetic field has a minimum, enabling the entrance of high-energy particles from space [40]. Given that satellites are exposed to high levels of radiation when they fly over this region [41], the SAA increases the noise in OMI-retrieved data in a significant fashion [24]. The remarkable difference in Figure 1 can be attributed to the photon energy being proportional to its frequency, which is greater by two orders of magnitude for the ultraviolet wavelengths with respect to the visible ones.

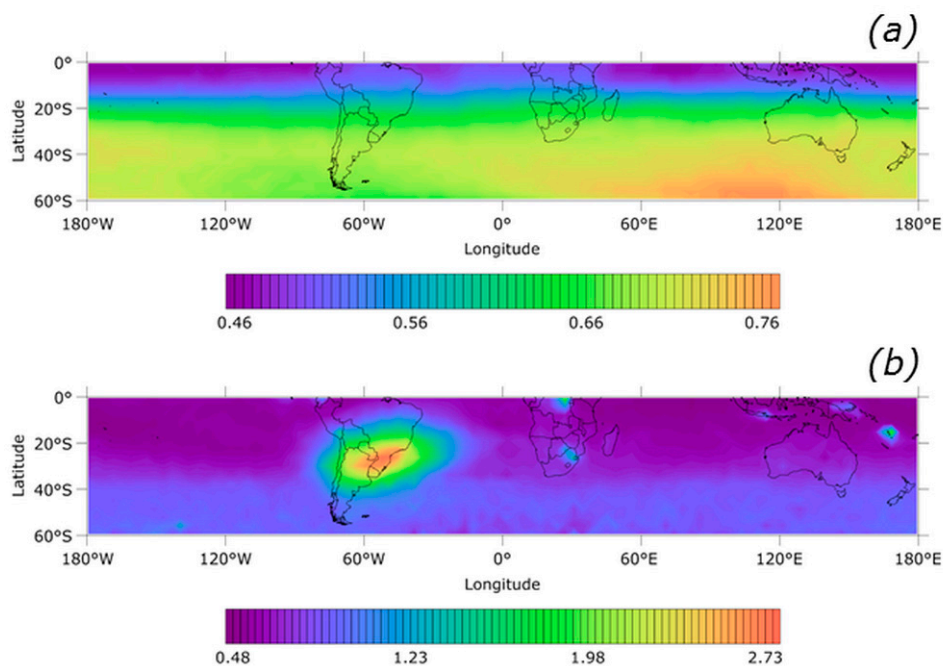


**Figure 1.** Mean concentrations for the quarterly (Q) time series over the study period for (a) NO<sub>2</sub> in the stratospheric (Strat) and (b) SO<sub>2</sub> in the planetary boundary layer (PBL). Values expressed in DU. The prominent mean concentrations in southern Brazil (BRA) in (b) are related to the South Atlantic Anomaly (SAA).

Standardised anomalies for each of the seasons and for the Q time series were built in order to homogenise the entire study region and to remove (or at least attenuate) the distortion created in the SAA region. Standardised anomalies are a useful tool to make sets of different data comparable to each

other. They have been used across a number of applications [42–44]. Figure S1 shows a loop for the DJF SO<sub>2</sub> standardised anomalies in the PBL. This is an example that shows how the simple procedure of using standardised anomalies removed the SAA signal, for it is not discernible in each of the figures of this loop. A trend analysis was carried out on the standardised anomalies for each of the seasons individually and for the Q time series. The trends for the standardised anomalies were calculated and statistically tested using a level of significance of 95%. These trends were rescaled by multiplying them by the corresponding SD in order to get a linear trend for the original seasonal concentrations. A rescaling was also applied to the statistic used to test the rescaled trends in order to assess the significance of the trends for the original variables. As pointed out in the Intergovernmental Panel on Climate Change's (IPCC) Fifth Assessment Report there is no physical reason for the time series to have a linear behaviour in time [45]. Apart from the linear trend analysis, the Mann-Kendall (MK) test [46], which evaluates the existence of monotonic upward or downward trends, were implemented on the standardised anomalies. According to [46] the test relies upon the calculation of the following quantity:

$$S = \sum_{j=1}^{n-1} \sum_{i=k+1}^n \text{sgn}(x_i - x_j), \quad (1)$$

In (1)  $n$  represents the number of points in each of the time series of standardised anomalies, and

$$\text{sgn}(x_i - x_j) = \begin{cases} -1 & \text{if } x_i < x_j \\ 0 & \text{if } x_i = x_j \\ 1 & \text{if } x_i > x_j \end{cases} \quad (2)$$

For  $n \geq 10$  (which is the case here) the normal approximation test is used, for which the value of the statistic  $Z$  is defined as

$$Z = \begin{cases} \frac{S-1}{\sqrt{\text{VAR}(S)}} & \text{if } S > 0 \\ 0 & \text{if } S = 0 \\ \frac{S+1}{\sqrt{\text{VAR}(S)}} & \text{if } S < 0 \end{cases} \quad (3)$$

In (3)  $\text{VAR}(S)$  stands for the variance of  $S$ , defined as  $\text{VAR}(S) = [n(n-1)(2n+5) - \sum_{p=1}^q t_p(t_p-1)(2n+5)]/18$  with  $q$  and  $t_p$  being the number of tied groups and the number of values in the  $p$ -th group, respectively [46]. Positive and negative values of  $Z$  indicate upward and downward trends, respectively. The value of (3) is compared against the critical value  $Z_c$  of a normal distribution, which depends upon the choice of the level of significance (e.g.,  $Z_c = 1.96$  for a level of significance of 95%). The results of the trend analyses are presented in the next section.

### 3. Results

#### 3.1. SO<sub>2</sub> Trends

##### 3.1.1. PBL

Seasonal SO<sub>2</sub> linear trends in the PBL are shown in Figure 2. Pixels with a significant trend are cross-hatched. Trend calculations were not carried out for grid cells that had at least one missing value. This is particularly relevant at the higher latitudes of the study region where the number of missing values is remarkable. Skipping the trend calculation in these cases avoids the estimation of potential spurious trends that may arise from time series with missing values at the beginning or the end of the study period. This is the reason why some panels of the figure show a lowermost blank latitudinal band, most notably in the JJA one (and consequently in the Q one) owing to polar night effects. Each of the panels was built using the same scale. Trends in the PBL range from  $-1.375$  to  $2.825$  DU decade<sup>-1</sup>, disregarding the season. Trends in the Q time series are smoother, ranging from  $-0.50$  to  $1.50$  DU decade<sup>-1</sup> (Figure 1a). Only 42 pixels (out of 10,686 analysed) have a significant linear trend.

Significant positive trends occur in central SA, to the east of the Democratic Republic of the Congo (COD), and over Vanuatu (VUT), and significant negative trends were seen in north-eastern Papua New Guinea (PNG). The significant positive trends in eastern COD and over VUT, approximately of  $1 \text{ DU decade}^{-1}$  and  $0.30 \text{ DU decade}^{-1}$ , respectively, are in line with an increase in annual  $\text{SO}_2$  emissions in the 2012–2014 period when compared with the 2005–2007 biennium [24]. Eastern COD has the largest concentration of significant adjoining points. Nyiamuragira and Nyiragongo are the two active volcanoes in the region that contribute to the emissions [47], the latter ranking among Africa's most active volcanoes [48] and classified as a "Decade" volcano [49]—i.e., a volcano that was particularly selected for studies due to its proneness to cause natural disasters. The significant negative trends in PNG are also in agreement with the existing literature, with several volcanoes contributing to these figures [50]. Overall, the hemispheric average trend (HAT) is just below  $0.08 \text{ DU decade}^{-1}$  if all 10,686 analysed points are considered, but it experiences a tenfold increase—to  $0.80 \text{ DU decade}^{-1}$ —if only the 42 pixels with a significant trend are included. In both cases these figures are in contradiction with the IPCC's predicted decrease in  $\text{SO}_2$  concentrations within the century [51].

Linear trends for the DJF quarter are shown in Figure 2b; they range from  $-0.80$  to  $2.60 \text{ DU decade}^{-1}$ . The number of analysed pixels is 13,982 with only 62 of them showing a significant linear trend. Like in the Q case, the HAT including only these points is much stronger ( $0.57 \text{ DU decade}^{-1}$ ) than that obtained by averaging the entire set of grid cells ( $0.07 \text{ DU decade}^{-1}$ ). As in Figure 2a, eastern COD shows a significant positive trend (of the order of  $0.60 \text{ DU decade}^{-1}$  in this case), whereas northern PNG shows a significant negative trend (approximately  $-0.60 \text{ DU decade}^{-1}$ ). Two new regions with a significant linear trend that were not present in Figure 2a appear over the eastern Indian Ocean, yet they are negligible when compared with the trends found over the continents. Overall, the region that has the largest increase in significant values occurs in SA, particularly over north-western Argentina (ARG) where the trends are in the order of  $0.30 \text{ DU decade}^{-1}$ . Trends in MAM (Figure 2c) range from  $-0.60$  and  $1.50 \text{ DU decade}^{-1}$ . The number of points with a significant trend reduces to 40 (out of 13,030 analysed pixels) with the location of them restricted to eastern COD and SA. Linear trends in the former region are in the order of  $1 \text{ DU decade}^{-1}$  on average. As to SA, positive and negative significant values occur: the most positive trends were over the south-eastern Brazilian coast (around  $1.30 \text{ DU decade}^{-1}$ ) while the most negative values (of the order of  $-0.30 \text{ DU decade}^{-1}$ ) were located approximately over the southernmost portion of the Province of Buenos Aires (ARG). Once again, the HAT estimated only using the pixels that have a significant value ( $0.90 \text{ DU decade}^{-1}$ ) is ten times greater than that using the entire set.

The season that has the maximum number of grid cells with a significant trend is JJA, accounting for 75 of them (out of 11,802 points) (Figure 2d). The HAT calculated using the significant points only is  $-0.14 \text{ DU decade}^{-1}$  but it reverses the sign and is approximately seven times weaker when the entire domain is used to estimate it. The two regions with significant values are the same that were present in MAM, but with the one in SA including a largest portion of their pixels with a significant trend in the South Atlantic coasts. Regarding eastern COD, the trend is again positive and in the order of  $2 \text{ DU decade}^{-1}$ , the strongest one for the season. However, the most dramatic effect occurs in the eastern coasts of SA, where pixels having negative trends account for the majority of the significant points, with an average trend of  $-0.60 \text{ DU decade}^{-1}$ . The number of pixels with a significant trend in SON accounts for 55 (out of 12,130) (Figure 2e). They consist of a single pixel in northern PNG ( $-0.70 \text{ DU decade}^{-1}$ ) and the rest of them in central SA, spanning the  $20^\circ\text{S}$ – $40^\circ\text{S}$  latitudinal band, with negative trends off the coast (approximately  $-0.60 \text{ DU decade}^{-1}$  on average) and positive ones over the landmass. Significance in eastern COD vanishes in this season. The strongest positive values in central SA are in the order of  $1 \text{ DU decade}^{-1}$ ; they take place in central Chile (CHL), where Santiago (SCL), one of Latin America's most polluted cities [52,53] is located. The dispersion of pollutants in central CHL is hindered by the presence of inversion layers associated with anticyclonic conditions, the effect of which can be seen in the trends across all the seasons and even in the Q case. However, if these subsidence-related inversions are a cause of the strongest SON trends there they are not the

only cause since these inversions are not more frequent during SON but span the entire year [52,53]. The HAT—considering the significant trends only—is almost  $0.60 \text{ DU decade}^{-1}$ ; this value is more than eleven times greater than that estimated using all the points.

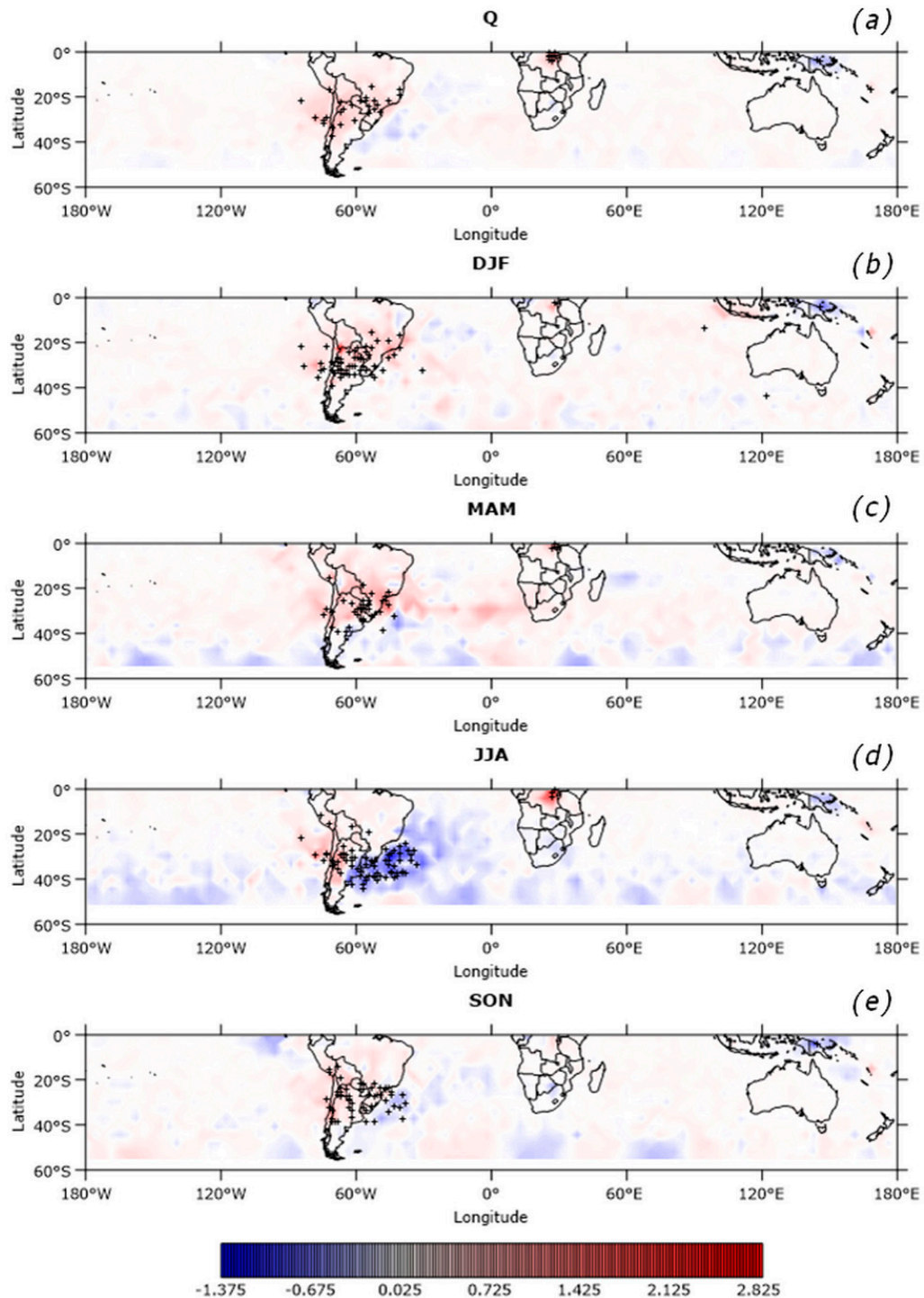


**Figure 2.** Linear trends (background colours) for the SO<sub>2</sub> seasonal concentrations in the planetary boundary layer (PBL) (in DU decade<sup>-1</sup>) for (a) Q, (b) December, January, February (DJF), (c) March, April, May (MAM), (d) June, July, August (JJA), and (e) September, October, November (SON). Significant trends are cross-hatched. The level of significance is 95%. Pixels that had at least a seasonal missing value were not included in the analysis.

### 3.1.2. TRL, TRM and STL

Unlike the SO<sub>2</sub> concentrations in the PBL, the linear trend analysis revealed significance at none of the pixels for the SO<sub>2</sub> seasonal concentrations in the TRL, TRM and the STL. Figures 3–5 show these non-significant linear trends in the SO<sub>2</sub> seasonal concentrations in the TRL, the TRM and the STL, respectively. These trends are expressed in DU century<sup>-1</sup> in view of their weakness. They range from −3.60 to 8.90, −1.51 to 8.24, and −1.35 and 5.15 DU century<sup>-1</sup> in the TRL, the TRM and the STL, respectively.

The most extreme linear trends in the TRL occur in JJA both for the positive and the negative values (Figure 3). The former ones occur in eastern COD (around 8 DU century<sup>-1</sup> on average) and the latter ones take place in the South Atlantic Ocean (SAO) off the Brazilian coasts (in the order of −3 DU century<sup>-1</sup> on average). In the case of the Q time series (Figure 3a) the number of pixels with a significant monotonic trend is 619 (out of 10,325) split into 555 and 64 for upward and downward trends, respectively (Table 1). These points do not extend beyond 42.5°S, and they are distributed as follows: 388 between 0°S and 20°S (i.e., the tropical band), 227 for the 20°S–40°S band (i.e., the subtropical band), and just 4 in the 40°S–60°S band (i.e., the high-latitude band). Furthermore, there are regions with a relatively small amount of these pixels, most notably northern Amazonia (NAM), the eastern Tropical Pacific off the coasts of Ecuador and Peru (PER), and the SAO. By contrast, there are regions that have a large concentration of such points, most notably the eastern Pacific off the coasts of northern CHL and southern PER, all of them with an upward trend, and northern PNG, with grid cells exhibiting a downward trend.

**Table 1.** Number of pixels with a significant monotonic trend (not necessarily linear) for the SO<sub>2</sub> seasonal concentrations in the lower troposphere (TRL).

| Latitudinal Band             | Q      | DJF    | MAM    | JJA    | SON    |
|------------------------------|--------|--------|--------|--------|--------|
| 0°S–20°S                     | 388    | 387    | 298    | 379    | 359    |
| 20°S–40°S                    | 227    | 573    | 387    | 454    | 382    |
| 40°S–60°S                    | 4      | 159    | 98     | 56     | 62     |
| <i>Total upward</i>          | 555    | 921    | 480    | 314    | 602    |
| <i>Total downward</i>        | 64     | 198    | 303    | 575    | 201    |
| <i>Total analysed pixels</i> | 10,325 | 13,490 | 12,706 | 11,551 | 11,693 |

The number of grid cells with a monotonic trend for the DJF time series increases to 1119 (out of 13,490) with 387, 573 and 159 of them filling the tropical, the subtropical and the high-latitude bands, respectively (Table 1). Furthermore, 921 (198) of these points are associated to an upward (downward) trend. The south Pacific and the south Atlantic oceans between 45°S and 60°S are the two most notable regions that are empty of these pixels (Figure 3b). On the other hand, the region with a greater number of contiguous points showing a monotonic downward trend is northern PNG; in contrast, the points with an upward trend seem to be evenly distributed across the Atlantic and the Pacific basins. Regarding the MAM time series, the number of pixels that have a trend is 783 (out of 12,706); 298, 387 and 98 occur in the tropical, the subtropical and the high-latitude bands, respectively (Table 1). The number of pixels with an upward (downward) trend is 480 (303). The most notable feature of this season is the dipole that is present in SA, with pixels showing a positive trend occurring in central SA and pixels with a negative trend located off the coasts of ARG. On the other hand, points with a significant monotonic trend at high latitudes are almost void in the south Pacific and the south Atlantic oceans (Figure 3c); these regions coincide with the void areas present in the DJF case.

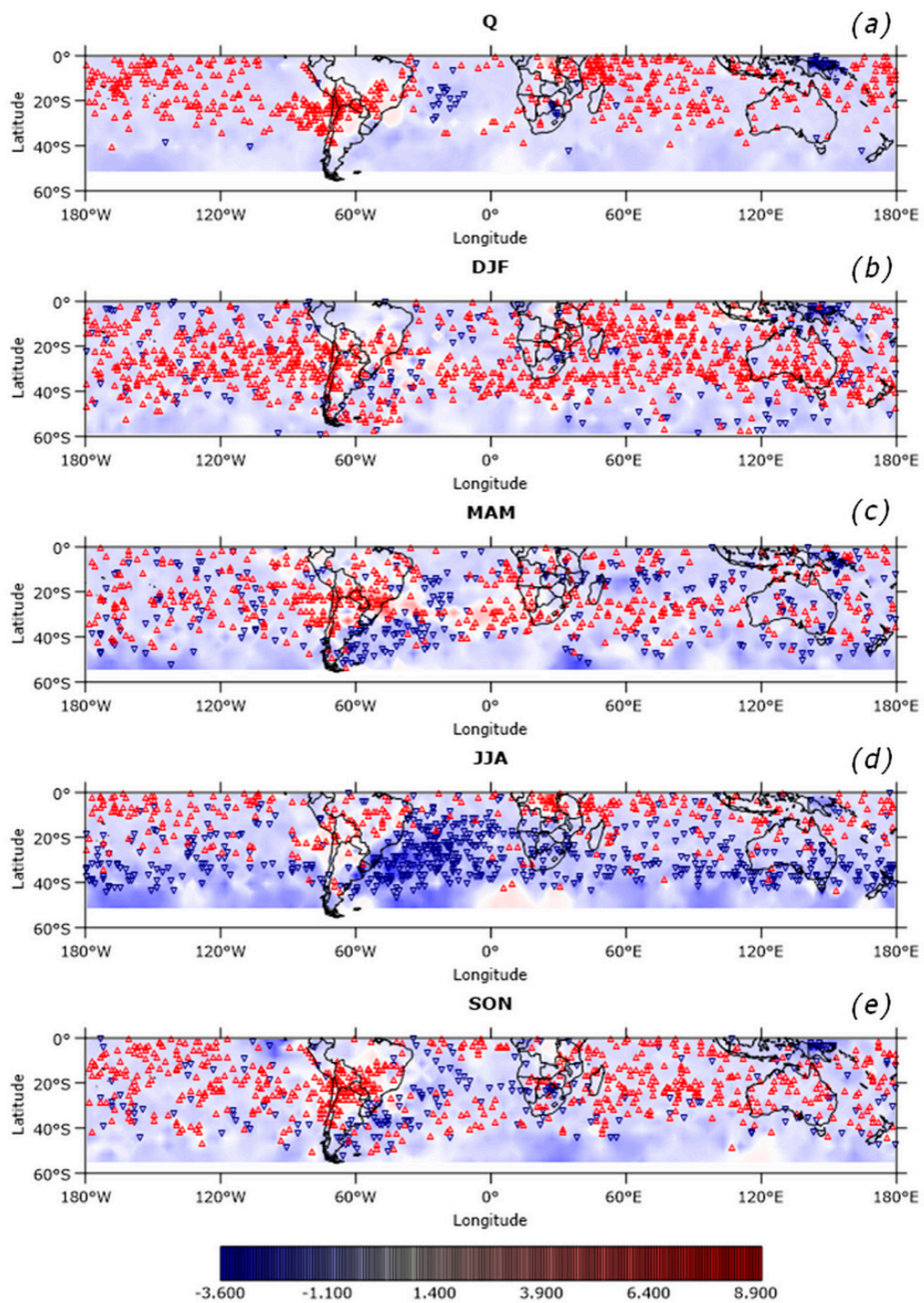


**Figure 3.** Linear trends (background colours) for the SO<sub>2</sub> seasonal concentrations in the lower troposphere (TRL) (in DU century<sup>-1</sup>) for (a) Q, (b) DJF, (c) MAM, (d) JJA, and (e) SON. Red and blue arrows mark the pixels that have a significant monotonic upward and downward trend (not necessarily linear), respectively. A level of significance of 95% was set. As in Figure 2, pixels whose time series had at least a seasonal missing value were not included in the analysis.

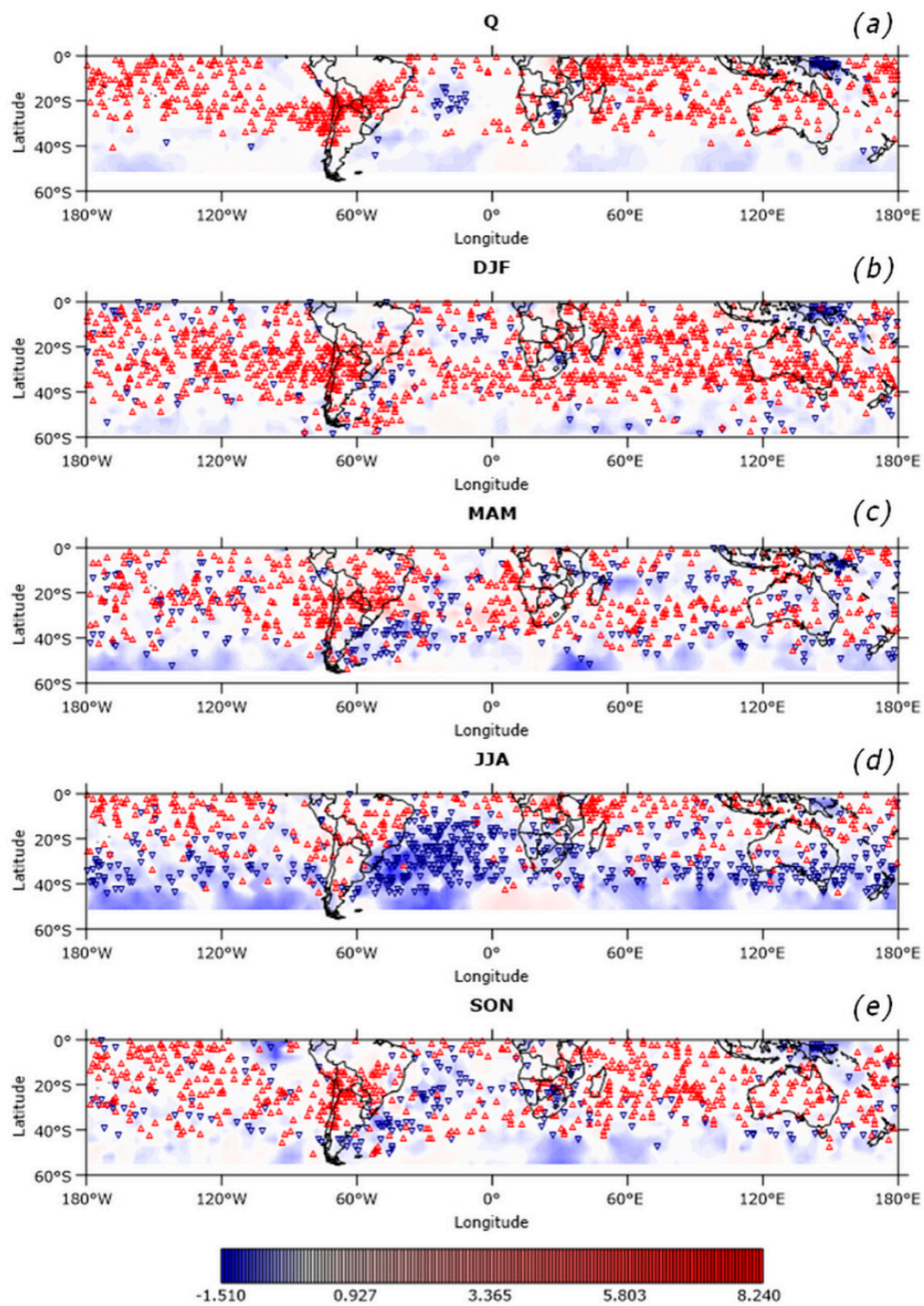


**Figure 4.** As in Figure 3 but for the SO<sub>2</sub> seasonal concentrations in the middle troposphere (TRM). Q, DJF, MAM, JJA and SON figures are shown in panels (a–e), respectively.

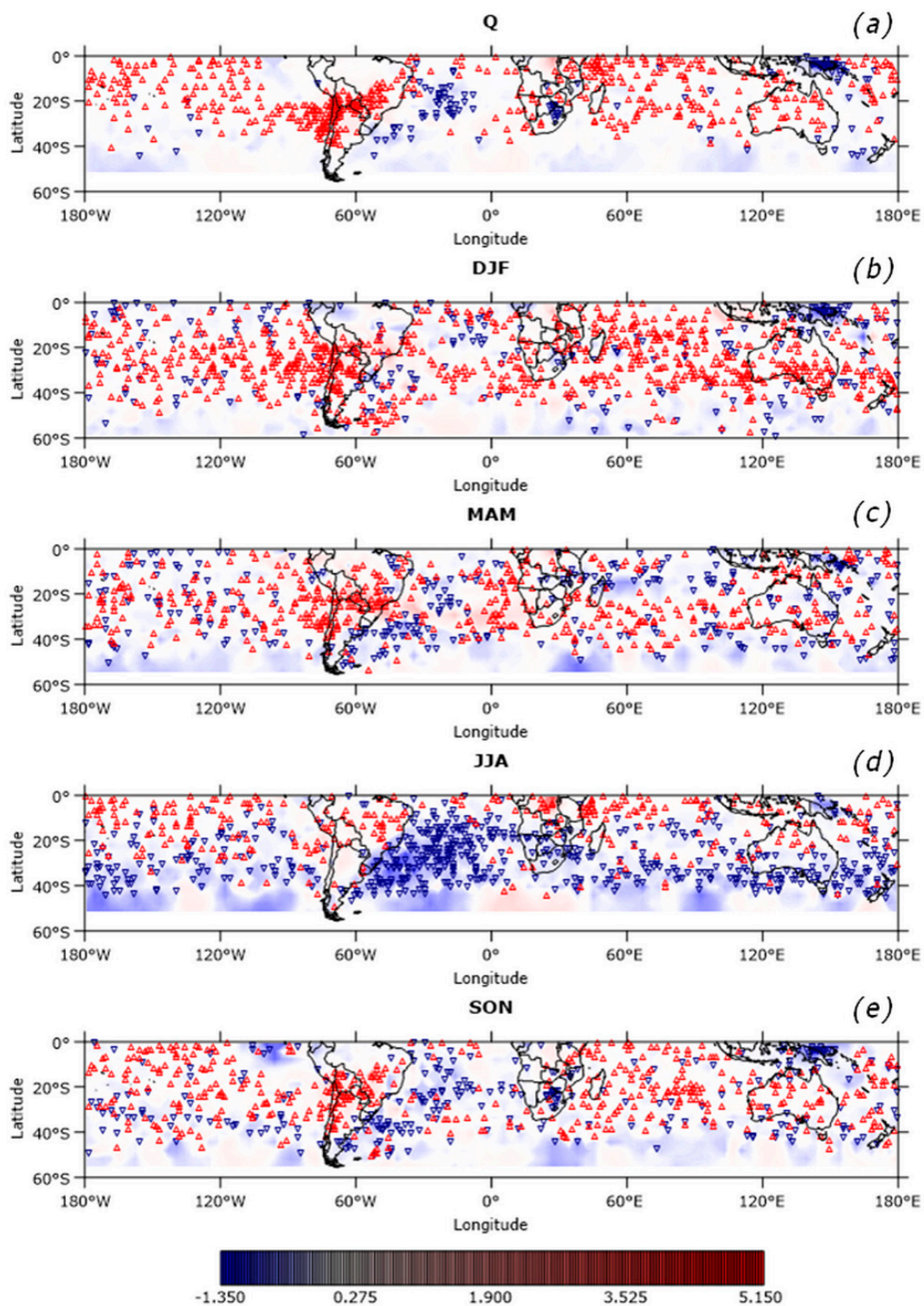


**Figure 5.** As in Figure 3 but for the SO<sub>2</sub> seasonal concentrations in the upper troposphere and the lower stratosphere (STL). Q, DJF, MAM, JJA and SON figures are shown in panels (a–e), respectively.

The JJA time series record 889 pixels (out of 11,551) with a significant monotonic trend, with the most number of them lying in the subtropical belt (454), followed by the tropical and the high-latitude bands with 379 and 56, respectively (Table 1). There are no pixels in such condition beyond 46.5°S. Even though north of this latitude all regions seem to be fairly populated, these points are particularly

dense in the eastern coast of SA and over the Atlantic, where there is a large region with pixels having a downward trend (Figure 3d). Actually, JJA is the only season that is dominated by points with such a characteristic and, in general, the subtropical (tropical) band seems to include the majority of the points with a downward (upward) trend. As for the SON quarter, the number of grid cells with a significant trend is 803 (out of 11,693), with the tropical and the subtropical bands including almost the same number (359 and 382, respectively), and the high-latitude band including the remainder with a count of just 62 (Table 1). In addition, three quarters of these pixels have an upward trend. The largest concentration of points with a monotonic trend takes place over central SA where the trends are upwards (Figure 3e).

The non-significant linear trends for the seasonal SO<sub>2</sub> concentrations in the TRM (Figure 4) are weaker than those in the TRL. The strongest negative values (in the order  $-1.50$  DU century<sup>-1</sup>) occur in DJF in north-eastern PNG, while the strongest positive ones (approximately 8 DU century<sup>-1</sup>) take place in SON in central BRA. Even though these trends are not significant, the latter result should be taken with caution as the effect of the SAA might not have been completely removed by the normalisation that was carried out on the variables, yet other effects cannot be ruled out. Notwithstanding, biomass burning in Amazonia traditionally peaks in September [54,55], and hotter fires can create their own convective systems so that the trace gases can be transported well into the higher troposphere ([55] and references therein).

The number of pixels with a significant monotonic trend in the Q time series is 736 (out of 10,359) with 666 representing an upward trend and the rest of them exhibiting the opposite trend (Table 2). The count of grid cells with a trend is greater in the tropical band with more than half of them located there, followed by the subtropical and the high-latitude bands. For the rest of the seasons the latitudinal band that has the greatest population of pixels with a significant trend is the subtropical one, followed by the tropical and the high-latitude bands.

**Table 2.** As in Table 1 but for the SO<sub>2</sub> concentrations in the TRM.

| Latitudinal Band             | Q      | DJF    | MAM    | JJA    | SON    |
|------------------------------|--------|--------|--------|--------|--------|
| 0°S–20°S                     | 439    | 399    | 324    | 394    | 333    |
| 20°S–40°S                    | 292    | 592    | 396    | 412    | 395    |
| 40°S–60°S                    | 5      | 148    | 93     | 62     | 66     |
| <i>Total upward</i>          | 666    | 956    | 555    | 362    | 592    |
| <i>Total downward</i>        | 70     | 183    | 258    | 506    | 202    |
| <i>Total analysed pixels</i> | 10,359 | 13,521 | 12,725 | 11,567 | 11,732 |

The largest density of pixels with a trend occurs in SA, from the northern coasts of CHL to southern BRA, extending along northern ARG (Figure 4a). They are associated with upward trends with the contribution of at least two volcanoes (Isluga in CHL and Sabancaya in PER) [24]. The 70 points that have a downward trend mainly locate over the Atlantic east of BRA, in eastern South Africa, and in northern PNG. In the last case, the contribution of several volcanoes with decaying activity in the recent years is documented [50]. On the other hand, NAM is another region with no pixels showing any trend at all, apart from those in the high latitudes.

The number of points with a significant trend in DJF is 1139 (out of 13,521) with 956 (183) having an upward (downward) trend. Most of them are distributed across the tropical and the subtropical latitudes. Apart from the high latitudes, NAM is again the region that has the least concentration of pixels in that condition, followed by the SAO (Figure 4b). By contrast, the regions that show the higher density of such pixels coincide with those present in the Q case, i.e., the region between northern CHL and southern BRA for upward trends and northern PNG for downward trends. Regarding MAM, the points that have a significant monotonic trend are 813 (out of 12,725) with 555 (258) of them having an upward (downward) trend. The largest concentration of grid cells showing an upward trend occurs in the same region than in the Q and the DJF cases, i.e., from central CHL to southern BRA across

northern ARG. By contrast, the least concentration of points with a trend occurs over the southern oceans. Unlike the Q and the DJF cases NAM does show points with a significant monotonic trend in this season, and their trend is upwards (Figure 4c). As to the JJA quarter, 868 pixels (out of 11,567) show a significant monotonic trend. They are split between 362 (506) points with an upward (downward) trend. As in the TRM case (cf. Table 1), this makes JJA the only season with the number of pixels having a downward trend exceeding their upward counterpart. Downward trends dominate the subtropical latitudes whereas upward trends abound in the tropical latitudes. The region that has the higher density of points with downward trends is the SAO and these pixels are in conjunction with negative linear trends that are the season's strongest negative ones (Figure 4d). In the case of SON, 794 pixels (out of 11,732) have a significant trend, 592 (202) of them exhibiting upward (downward) trends. Most of these points are scattered across the tropical and the subtropical latitudes. The region that has a relative larger concentration of pixels with a significant monotonic trend is the same as in the Q case, i.e., the region that extends from the northern coasts of CHL to southern BRA across northern ARG, conjoined with positive linear trends (Figure 4e).

The non-significant linear trends for the SO<sub>2</sub> seasonal concentrations in the STL are shown in Figure 5. These linear trends are also expressed in DU century<sup>-1</sup>. They range from -1.35 to 5.15 DU century<sup>-1</sup> considering individual points. The regions that have the average strongest positive and negative linear trends are Amazonia (approximately 4.40 DU century<sup>-1</sup>) and northern PNG (around -1.30 DU century<sup>-1</sup>), respectively, both in the SON quarter.

The count of pixels with a significant monotonic trend in the Q time series is 619 (out of 10,379), split between 495 and 124 for the upward and the downward trends, respectively (Table 3). Most of these points are distributed across the tropical latitudes, followed by the subtropical and the high-latitude bands. As with the previous layers, the higher number of points with a significant trend shifts from the tropical to the subtropical band for the rest of the seasons. The location of the most concentration of points with upward and downward trends in the Q case is similar to that of the TRM's counterpart (Figure 5a, cf. Figure 4a).

**Table 3.** As in Table 1 but for the SO<sub>2</sub> concentrations in the STL.

| Latitudinal Band             | Q      | DJF    | MAM    | JJA    | SON    |
|------------------------------|--------|--------|--------|--------|--------|
| 0°S–20°S                     | 339    | 345    | 304    | 368    | 280    |
| 20°S–40°S                    | 270    | 502    | 393    | 417    | 367    |
| 40°S–60°S                    | 10     | 140    | 84     | 65     | 68     |
| <i>Total upward</i>          | 495    | 768    | 487    | 300    | 450    |
| <i>Total downward</i>        | 124    | 219    | 294    | 550    | 265    |
| <i>Total analysed pixels</i> | 10,379 | 13,554 | 12,734 | 11,590 | 11,747 |

Regarding the DJF time series, the number of grid cells with a significant trend is 987 (out of 13,554), with 768 (219) of them exhibiting an upward (downward) trend. The highest density of points with an upward monotonic trend occurs over central ARG and CHL; this region is associated with upward linear trends. On the other hand, the location of the highest concentration of pixels with a downward trend is once again northern PNG and they are conjoined to negative linear trends (Figure 5b). As to MAM, the count of points with an upward (downward) trend is 487 (294), out of a total of 12,734. The location that has the most concentration of pixels with an upward trend in this season seems to replicate the DJF's one, yet with a thin zonal line of disruption across approximately 30°S; the higher density of points with a significant downward trend occurs in the SAO east of the Argentine coasts. In both cases these pixels are in compliance with their corresponding linear trends (Figure 5c). The matter concerning the downward trends is more exaggerated in JJA where these pixels span a much larger region than in the MAM's case (Figure 5d). As before (cf. Tables 1 and 2), JJA is the only season with the number of points having a downward trend exceeding that with an upward trend (Table 3). Concerning the SON quarter, the count of points with a significant trend stands at

715 (out of 11,747), split into 450 (265) with an upward (downward) trend. The regions that have the largest concentration of pixels with an upward and downward trends coincide with the ones in the Q counterpart and they are in correspondence with their linear trends (Figure 5e).

### 3.2. NO<sub>2</sub> Trends

The linear trends for the seasonal time series of Trop and Strat NO<sub>2</sub> concentrations and the pixels that show a monotonic upward or downward trend for the standardised anomalies of the same variables are shown in Figures 6 and 7, respectively. As with the SO<sub>2</sub> seasonal concentrations in most of the layers of the atmosphere all these linear trends are not significant across the analysed seasons both in the Trop and the Strat. In the former layer the linear trends range from  $-3.25$  to  $2.50$  DU century<sup>-1</sup> (Figure 6) and they are weaker in the latter layer, ranging from  $-1.184$  to  $0.363$  DU century<sup>-1</sup> (Figure 7).

Unlike the SO<sub>2</sub> case the number of pixels with a monotonic upward trend in the Trop is the dominant characteristic in all the seasons (Figure 6), with the maximum number of them (7954 out of 8095) taking place in the Q time series (Table 4)—they are largely concentrated in the subtropical and high-latitude bands over the oceans. On the other hand, MAM is the season that shows the largest number of pixels exhibiting a monotonic downward trend, with these points being mainly distributed across the tropical latitudes but with a large concentration of them also taking place in southern SA (Figure 6c). Despite this, grid cells with an upward trend are by far the most dominant in all the seasons. These results are quite in agreement with an overall increase in the global tropospheric NO<sub>2</sub> concentrations in the recent years [56]. The regions exhibiting positive and negative monotonic trends in all the seasons are in correspondence with the linear trends shown at these locations. According to [57] the months of maximum NO<sub>2</sub> concentrations over central SA/Amazonia, southern Africa and northern Australia (AUS) take place in the SON quarter. There are pixels with a significant monotonic trend in these regions within the specified season, with southern Africa and large portions of central SA/Amazonia exhibiting upward trends and northern AUS exhibiting downward trends; the presence of downward trends in western Amazonia is noteworthy as well (Figure 6e). The upward trends are evidence that the emissions in the corresponding regions increased in the analysed period, and the converse situation occurs for the downward trends, most notably in northern AUS. Unfortunately, no further links of this kind can be established for the rest of the seasons as much of the maximum NO<sub>2</sub> concentrations in the SH take place during SON.

The lack of previous research covering the topics dealt with in our paper does not permit direct comparison at a hemispheric scale. However, trends for tropospheric NO<sub>2</sub> concentrations were presented at major urban agglomerations in the SH [26]. According to Figure 6a the monotonic upward trends in Lima and SCL are in qualitative match with the results presented in [33] as they are in Jakarta and Sydney for a downward trend, whereas they do not match in Buenos Aires, Johannesburg, San Pablo and Rio de Janeiro, as the monotonic trends at these cities are not significant. The case of Sydney is interesting since Figure 6a shows that the only pixel with a significant downward trend in the region is located at this city.

The fact that the standardised seasonal NO<sub>2</sub> Strat concentrations time series have no pixels with a monotonic upward trend for any of the analysed seasons is the most striking feature of this paper. The Q time series have the least number of points exhibiting a downward trend with a count of just 70 (Table 5) that are located in the subtropical latitudes (Figure 7a). This number increases to 6042 for DJF with most of these pixels distributed across the subtropical and the high-latitude bands but with blanks in several zones, most notably in the southern SAO (Figure 7b). MAM is the season that has the largest number of pixels with a monotonic trend with a count of 10,292, most of them beyond 20°S with a noticeable blank region at high latitudes south of AUS (Figure 7c). A feature of the Q, the DJF and the MAM time series is that there are virtually no points with upward linear trends. This is not the case for JJA and SON (Figure 7d,e, respectively) whose count of pixels with a monotonic trend reduces dramatically to 1168 and 372, respectively.

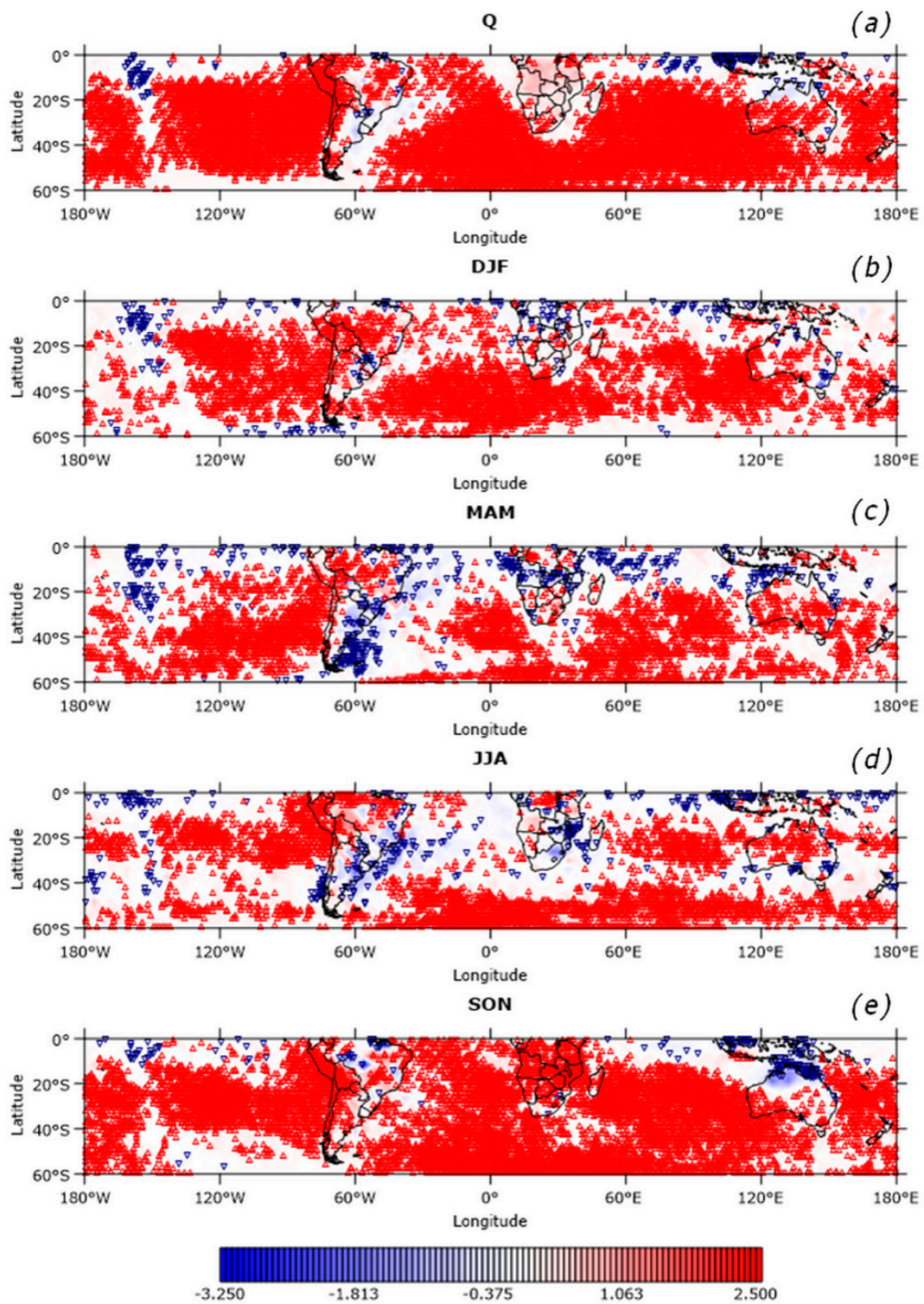


**Figure 6.** As in Figure 3 but for the seasonal concentrations of NO<sub>2</sub> in the troposphere (Trop). Q, DJF, MAM, JJA and SON figures are shown in panels (a–e), respectively.

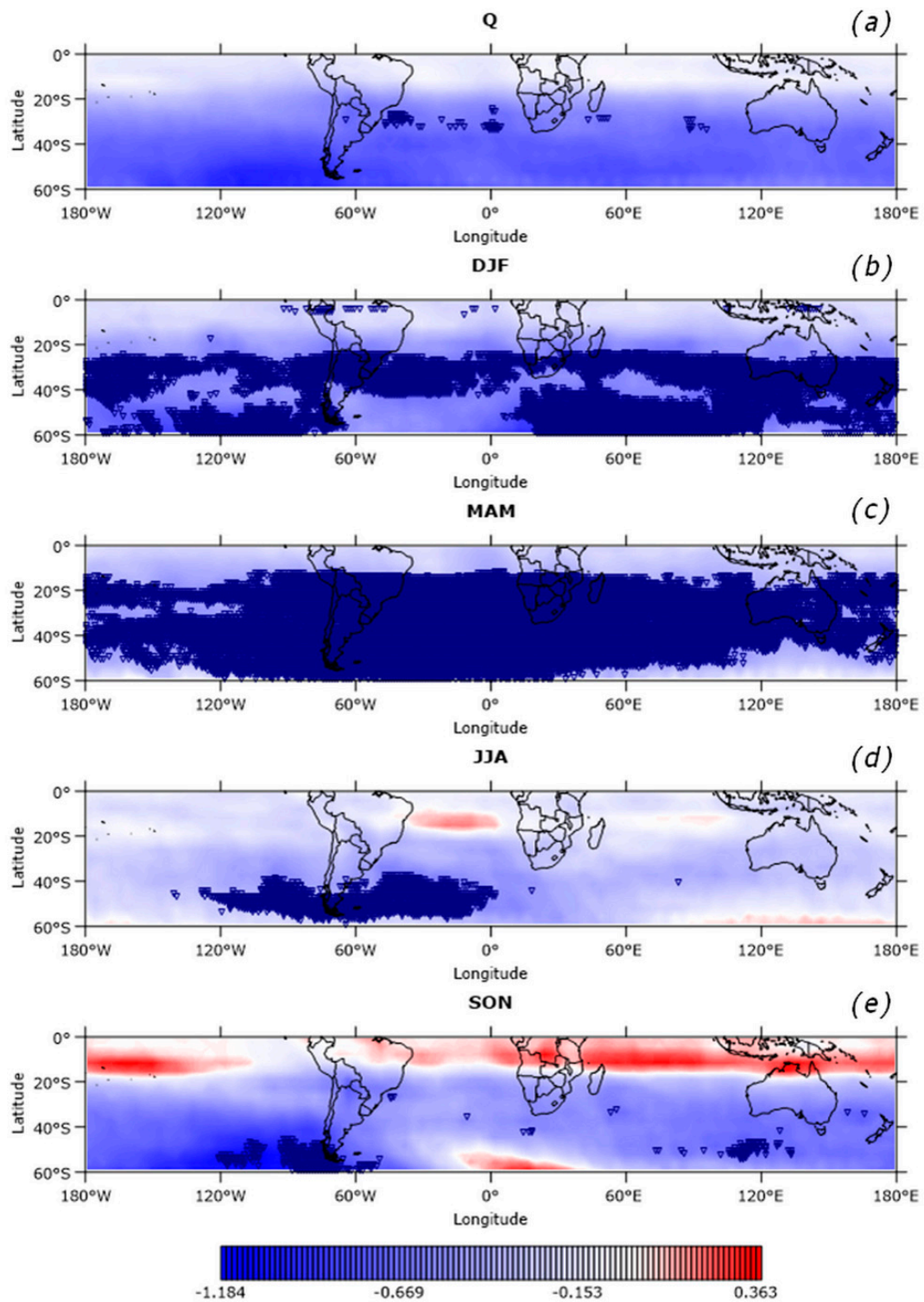


**Figure 7.** As in Figure 3 but for the seasonal concentrations of NO<sub>2</sub> in the stratosphere (Strat). Q, DJF, MAM, JJA and SON figures are shown in panels (a–e), respectively.

**Table 4.** As in Table 1 but for the NO<sub>2</sub> concentrations in the Trop.

| Latitudinal Band             | Q      | DJF    | MAM    | JJA    | SON    |
|------------------------------|--------|--------|--------|--------|--------|
| 0°S–20°S                     | 1455   | 792    | 650    | 938    | 1630   |
| 20°S–40°S                    | 3382   | 1883   | 1575   | 1031   | 3144   |
| 40°S–60°S                    | 3258   | 1641   | 1715   | 1838   | 2459   |
| <i>Total upward</i>          | 7954   | 4108   | 3472   | 3461   | 7054   |
| <i>Total downward</i>        | 141    | 208    | 468    | 346    | 179    |
| <i>Total analysed pixels</i> | 17,280 | 17,280 | 17,280 | 17,280 | 17,280 |

**Table 5.** As in Table 1 but for the NO<sub>2</sub> concentrations in the Strat.

| Latitudinal Band             | Q      | DJF    | MAM    | JJA    | SON    |
|------------------------------|--------|--------|--------|--------|--------|
| 0°S–20°S                     | 0      | 47     | 1338   | 0      | 0      |
| 20°S–40°S                    | 70     | 3179   | 5172   | 48     | 8      |
| 40°S–60°S                    | 0      | 2816   | 3782   | 1120   | 364    |
| <i>Total upward</i>          | 0      | 0      | 0      | 0      | 0      |
| <i>Total downward</i>        | 70     | 6042   | 10292  | 1168   | 372    |
| <i>Total analysed pixels</i> | 17,280 | 17,280 | 17,280 | 17,280 | 17,280 |

#### 4. Discussion

The prevailing meteorological conditions were briefly mentioned as a cause of SCL being a pollution-prone city. These conditions, along with other factors (such as topography) may conspire to make other regions of the world as polluted as, or even more polluted than, SCL, either seasonally or on an annual basis. Notwithstanding, the degree of relationship between concentrations and emissions is in general not as straightforward as this example suggests. This can be figured out from the trends observed in remote areas over open waters of the SH where there are no sources and the pollutants owe their existence to atmospheric transport. The number of research efforts devoted to identifying different linkages between the concentration of pollutants and the meteorological conditions is on the rise in both hemispheres, but they are more numerous in the Northern Hemisphere due to a number of factors that include this hemisphere having a large number of megacities, and therefore the highest concentration of regions with strong industrial activity. Even though the areas closer to the sources of pollutants (natural or anthropogenic) are expected to be the most affected by the emissions, the local and regional meteorology, the general circulation [58,59] and the chemistry should be considered altogether in order to establish the spatial extent of the influence and the actual concentrations. Recently, a study carried out for China found that the discrepancy in the relative values of the emissions and the SO<sub>2</sub> concentrations in the lower troposphere owing to a change in local meteorological conditions can represent up to 20–30%. Under the same scenario, the deviations from a linear relationship linking the emissions and the columnar concentrations can be up to 50% [60]. A similar study for the NO<sub>x</sub> regarding trends showed that meteorology may account for up to a 30% difference in emission/concentration differences [61]. More generally, the characteristics of the emissions—e.g., increase or decrease over time, seasonality—combined with a global warming scenario that leads to the alteration of the meteorological conditions may have an impact on the evolution of the concentrations and hence on the observed trends. The expansion of the tropical belt, the intensification of the Hadley Cell (HC) and the strengthening of upper tropospheric jets (UTJs) are part of the meteorological aspects of the global warming scenario that may play a role in the distribution of these pollutants, thereby modulating their concentrations across both hemispheres.

This work focused on the SH. The count of analysed pixels across all the seasons covered the entire study region for the NO<sub>2</sub> concentrations both in the troposphere and in the stratosphere. This was not the case for the SO<sub>2</sub> concentrations in the different analysed atmospheric layers owing to missing data. Our results show that there is a marked seasonality in the characteristics of the linear and non-linear trends over the SAO for the SO<sub>2</sub> concentrations, and in the sub-tropics and the

mid-latitudes for the NO<sub>2</sub> concentrations. In particular, both the linear and the non-linear trends in the SO<sub>2</sub> concentrations—and to a lesser extent in the NO<sub>2</sub> concentrations—over the SAO exhibit a general reversion in their condition in JJA with respect to the rest of the seasons (including the Q case), from upward to downward.

As mentioned above, the overall features in the global distribution of the seasonal SO<sub>2</sub> concentration trends can be at least partly interpreted by recalling some components of the large-scale circulation and their evolution in the recent years. A noteworthy distinction of these trends is the absence of significance in the linear trends in NAM in Figure 2 and in the monotonic non-linear trends in the same region in Figures 3–5, for the Q case as well as for the DJF and the SON seasons in all these sets of figures. This can be due to the effects of the HC's ascending branch, whose vigorous vertical currents remove the specie from the equatorial latitudes and deposits it in the descending regions, located around 30°S on average, where the concentration of significant trends is considerable. Taking into account the described mechanism, the upward trends found in the sub-tropical latitudes of SA can be attributed to two distinct effects: (a) increasing emissions and (b) intensification of the HC. The intensification of the HC has been proven in [62] and it is present in different reanalysis datasets from 1979 through 2009. It is a plausible explanation for what is observed, provided the intensification of the HC is also valid within our study period. Although not statistically different from zero, the background linear trends in NAM shown in Figures 3–5 are worth mentioning as they are consistent with a removal of this specific pollutant there. Grid cells with a significant positive non-linear trend in SA reach their southernmost position in DJF in concordance with the descending branch of the HC occupying its most poleward position during the summer months [62]. This agreement reinforces the intensification of the HC as a plausible mechanism for the latitudinal distribution of the observed trends. The poleward extent of the HC depends upon a number of land-sea contrast parameters—most notably the meridional temperature gradient—and moisture content [63] and so does the southernmost position of the significant trends. The relationship is complex, however, since the expansion of the tropical belt seems to have a dependence on the state of some modes of variability of the coupled atmosphere/ocean system, which in turn seems to depend on the concentration of anthropogenic aerosols [64]. The study of SO<sub>2</sub> concentrations in the SH is particularly important to this topic considering the effects SO<sub>2</sub> has on ozone depletion and the role played by the polar stratospheric ozone depletion in driving the widening of the tropical belt [65,66].

The importance of the UTJs to synoptic processes is that they drive the location of the storm tracks through baroclinic instability, but they also play a role acting as waveguides or inhibiting the poleward transport of wave activity [67], therefore interfering with the meridional circulation described above. The latitudinal distribution of the trends can be partly ascribed to the semi-horizontal transport of the pollutants away from their sources aided by the UTJs and redistributed by the eddy perturbations they contribute to create. UTJs are stronger in the winter hemisphere [68] thus creating more favourable conditions for baroclinic perturbations to develop. Generally speaking, the widening of the tropical belt implies an intensification (weakening) of the polar (subtropical) UTJ in DJF, and the converse situation takes place for JJA, i.e., the subtropical (polar) UTJ experiences a strengthening (weakening), yet the regions exhibiting significance are much more reduced [68]. Particularly over SA, the subtropical UTJ shows upward linear trends in both seasons [68] and this feature can be used to easily interpret the linear trends in PBL SO<sub>2</sub> concentrations for JJA (Figure 2d). Indeed, a strengthened UTJ has the potential to create more intense storm tracks, and the region in the SAO concentrating the downward trends is located in one of the most cyclogenetic regions of the SH, particularly during JJA [67].

The clockwise rotation of these low pressure systems removes the pollutants from the oceanic regions and accumulates them east of the Andes so that the positive trends there are also in agreement with this mechanism. Regarding the non-linear downward trends, the highest concentration of them in the SAO during JJA (Figures 3d, 4d and 5d) may respond to a chemical process combined with the aforementioned changing atmospheric conditions. The oxidation of SO<sub>2</sub> in the troposphere is at its maximum in the winter months [69]. Furthermore, due to its high aqueous solubility [70],

the production of sulphates via in-cloud oxidation of  $\text{SO}_2$  has been reported to be important [71,72]. The intensification of the subtropical UTJ in the SAO region from central SA to southern Africa during JJA impact on both the frequency and the strength of the storm tracks there, with both characteristics expected to increase, leading to more cloudiness and hence more proneness to in-cloud oxidation of the  $\text{SO}_2$ . Upward trends in the column of integrated water vapour content over the oceans in most of the regions of interest [45] are in concordance with the proposed mechanisms. The strengthening of the subtropical UTJ is also seen in the southern Indian Ocean from southern Africa to AUS [68], and the neighbouring regions exhibit non-linear downward trends in  $\text{SO}_2$  concentrations as well. A similar situation is also observed over New Zealand. There are no reasons for not to consider the same meteorological mechanisms for the  $\text{NO}_2$  trends. Concerning this particular pollutant, significant downward trends are generally closer to the landmasses—i.e., closer to the emission sources when compared with their  $\text{SO}_2$  counterparts. This may respond either to an actual reduction in the emissions or to the fact that  $\text{NO}_2$  has a lifetime of a few minutes against photolysis, leading to the generation of  $\text{O}_3$  [73], another tropospheric pollutant. In general, both  $\text{NO}_2$  and  $\text{SO}_2$  react with OH in polluted atmospheres, leading to the production of acids—it actually constitutes the dominant loss mechanism for  $\text{NO}_x$  and the removal is much more efficient for the  $\text{NO}_x$  species than it is for the  $\text{SO}_2$  [70]. The benefits of having a downward trend in both  $\text{SO}_2$  and  $\text{NO}_2$  concentrations at certain regions may be only apparent, as their reduction may imply these two compounds are oxidising and leading to the potential formation of acid rain.

## 5. Conclusions

The seasonal standardised anomalies of sulphur dioxide ( $\text{SO}_2$ ) and nitrogen dioxide ( $\text{NO}_2$ ) concentrations in different layers of the atmosphere were analysed for linear and non-linear trends in order to address the behaviour of these two pollutants in the context of a changing climate. The studied region was the Southern Hemisphere (SH) between the Equator and  $60^\circ\text{S}$ , the analysed period was 2004–2016, and Ozone Monitoring Instrument (OMI) data was used for both gases. To the best of our knowledge this is the first time the characterisation of non-linear trends was carried out in the entire SH. Standardisation was carried out as a twofold purpose: to remove (or at least attenuate) the known influence of the South Atlantic Anomaly in OMI data and to homogenise the datasets in the entire domain. On the one hand, linear trends were estimated and statistically tested. This procedure was carried out on the standardised anomalies of seasonal  $\text{SO}_2$  concentrations in the planetary boundary layer (PBL), the lower troposphere (TRL), the middle troposphere (TRM) and the upper troposphere and the lower stratosphere (STL), and  $\text{NO}_2$  concentrations in the troposphere (Trop) and the stratosphere (Strat), for the austral summer (DJF), autumn (MAM), winter (JJA) and spring (SON) time series, as well as for the quarterly (Q) time series. The obtained linear trends for the standardised anomalies were converted so that the trends for the original time series could be informed. On the other hand, non-linear trends were estimated for the series of standardised anomalies by means of the Mann-Kendall test and it was assessed whether the grid cells had a significant monotonic upward or downward trend.

The main findings of this paper can be summarised as follows. The  $\text{SO}_2$  concentrations show significant linear trends in the PBL only, but just a few pixels located mainly over the landmasses display such behaviour. The location of such pixels and their trends are in general in agreement with the existing literature. Even though an important number of grid cells in the TRL, the TRM, and the STL do not have significant linear trends, they exhibit significant monotonic upward or downward trends depending upon the region and the seasons considered, both over the landmasses and in remote regions over the oceans. A noteworthy feature is that JJA shows a large number of points with a downward trend in all the layers, while the opposite holds for the rest of the seasons. Concerning the  $\text{NO}_2$  concentrations, no significant linear trends were found either in the troposphere or in the stratosphere, but the former (latter) layer shows monotonic upward (downward) trends. Results are in agreement with a general increase in  $\text{NO}_2$  and  $\text{SO}_2$  emissions in the recent years [74,75] but they are

not in accordance with the predicted emissions for these two gases within the different scenarios of climate change for the current century. The presence of trends in remote areas of the hemisphere away from the sources (which are mostly located in the landmasses) suggests that the general circulation combined with local processes—both subject to climate change—and chemistry play an important role in the transport and the spatial distribution of these pollutants. The statistic used to test the significance of the monotonic upward or downward trends revealed different degrees of non-linearities but the exact types of these non-linear evolutions were not addressed. The determination of the most suitable function to fit will likely help in further understanding the way the concentrations of these two gases will behave in the future. This is a matter for future investigation.

**Supplementary Materials:** The following are available online at [www.mdpi.com/2072-4292/9/9/891/s1](http://www.mdpi.com/2072-4292/9/9/891/s1). Figure S1: Loop of standardised anomalies of PBL SO<sub>2</sub> concentrations in DJF. Significant values are cross-hatched; the number of them is shown in parenthesis. The level of significance was set to 95%.

**Acknowledgments:** We gratefully acknowledge the academic editor and three anonymous reviewers for their valuable comments and suggestions. PIP 2012–2014 N° 0075, PICT 2012–2027 and PIDDEF 2014 N° 26 grants partly funded this paper. The funds for covering the costs to publish in open access were provided by the Facultad Regional Buenos Aires of the Universidad Tecnológica Nacional.

**Author Contributions:** A.Y. and S.G.L. conceived the underlying ideas; A.Y. performed the calculations and the figures; A.Y. and S.G.L. analysed the data; A.Y. and S.G.L. wrote the paper. All the authors reviewed the manuscript.

**Conflicts of Interest:** The authors declare no conflict of interest. The founding sponsors had no role in the design of the study; in the collection, analyses, or interpretation of data; in the writing of the manuscript, and in the decision to publish the results.

## References

1. Myhre, G.; Shindell, G.D.; Bréon, F.-M.; Collins, W.; Fuglestedt, J.; Koch, D.; Lamarque, J.-F.; Lee, D.; Mendoza, B.; Nakajima, T.; et al. Anthropogenic and Natural Radiative Forcing. In *Climate Change 2013: The Physical Science Basis. Contribution of Working Group I to the Fifth Assessment Report of the Intergovernmental Panel on Climate Change*; Stocker, T.F., Qin, D., Plattner, G.-K., Tignor, M., Allen, S.K., Boschung, J., Nauels, A., Xia, Y., Bex, V., Midgley, P.M., Eds.; Cambridge University Press: New York, NY, USA, 2013; pp. 659–740.
2. Lohmann, U.; Feichter, J. Can the direct and semi-direct aerosol effect compete with the indirect effect on a global scale? *Geophys. Res. Lett.* **2001**, *28*, 159–161. [[CrossRef](#)]
3. Johnson, B.T.; Shine, K.P.; Forster, P.M. The semi-direct aerosol effect: Impact of absorbing aerosols on marine stratocumulus. *Q. J. R. Meteorol. Soc.* **2005**, *130*, 1407–1422. [[CrossRef](#)]
4. Lohmann, U.; Feichter, J. Global indirect aerosol effects: A review. *Atmos. Chem. Phys.* **2005**, *5*, 715–737. [[CrossRef](#)]
5. Ghan, S.J.; Liu, X.; Easter, C.; Zaveri, R.; Rasch, P.J.; Yoon, J.-H. Toward a Minimal Representation of Aerosols in Climate Models: Comparative Decomposition of Aerosol Direct, Semidirect, and Indirect Radiative Forcing. *J. Clim.* **2012**, *25*, 6461–6476. [[CrossRef](#)]
6. Mahowald, N.M.; Scanza, R.; Brahney, J.; Goodale, C.L.; Hess, P.G.; Moore, J.K.; Neff, J. Aerosol Deposition Impacts on Land and Ocean Carbon Cycles. *Curr. Clim. Chang. Rep.* **2017**, *3*, 16–31. [[CrossRef](#)]
7. Martin, J.H.; Fitzwater, S.E. Iron deficiency limits phytoplankton growth in the northeast Pacific subarctic. *Nature* **1988**, *331*, 341–343. [[CrossRef](#)]
8. Okin, G.; Mahowald, N.; Chadwick, O.; Artaxo, P. Impact of desert dust on the biogeochemistry of phosphorus in terrestrial ecosystems. *Glob. Biogeochem. Cycles* **2004**, *18*, GB2005. [[CrossRef](#)]
9. Stier, P.; Feichter, J.; Roeckner, E.; Kloster, S.; Esch, M. The evolution of the global aerosol system in a transient climate simulation from 1860 to 2100. *Atmos. Chem. Phys.* **2006**, *6*, 3059–3076. [[CrossRef](#)]
10. Kiros, F.; Shakya, K.M.; Rupakheti, M.; Regmi, R.P.; Maharjan, R.; Byanju, R.M.; Naja, M.; Mahata, K.; Kathayat, B.; Peltier, R.E. Variability of Anthropogenic Gases: Nitrogen Oxides, Sulfur Dioxide, Ozone and Ammonia in Kathmandu Valley, Nepal. *Aerosol Air Qual. Res.* **2016**, *16*, 3088–3101. [[CrossRef](#)]
11. Krotkov, N.A.; McLinden, C.A.; Li, C.; Lamsal, L.N.; Celarier, E.A.; Marchenko, S.V.; Swartz, W.H.; Bucsela, E.J.; Joiner, J.; Duncan, B.N.; et al. Aura OMI observations of regional SO<sub>2</sub> and NO<sub>2</sub> pollution changes from 2005 to 2015. *Atmos. Chem. Phys.* **2016**, *16*, 4605–4629. [[CrossRef](#)]

12. Jaffe, D.A.; Weiss-Penzias, P.S. Nitrogen Cycle. In *Encyclopedia of Atmospheric Sciences*; Holton, J.R., Curry, J.A., Pyle, J.A., Eds.; Academic Press: London, UK, 2003; Volume 1, pp. 205–213.
13. Bucsela, E.J.; Krotkov, N.A.; Celarier, E.A.; Lamsal, L.N.; Swartz, W.H.; Bhartia, P.K.; Boersma, K.F.; Veefkind, J.P.; Gleason, J.F.; Pickering, K.E. A new stratospheric and tropospheric NO<sub>2</sub> retrieval algorithm for nadir-viewing satellite instruments: Applications to OMI. *Atmos. Meas. Tech.* **2013**, *6*, 2607–2626. [[CrossRef](#)]
14. Kondo, Y. Reactive Nitrogen (NO<sub>x</sub> and NO<sub>y</sub>). In *Encyclopedia of Atmospheric Sciences*; Holton, J.R., Curry, J.A., Pyle, J.A., Eds.; Academic Press: London, UK, 2003; Volume 5, pp. 2193–2202.
15. Seinfeld, J.H. Tropospheric Chemistry and Composition: Aerosols/Particles. In *Encyclopedia of Atmospheric Sciences*; Holton, J.R., Curry, J.A., Pyle, J.A., Eds.; Academic Press: London, UK, 2003; Volume 6, pp. 2349–2354.
16. Yang, K.; Krotkov, N.A.; Krueger, A.J.; Carn, S.A.; Bhartia, P.K.; Levelt, P.F. Retrieval of large volcanic SO<sub>2</sub> columns from the Aura Ozone Monitoring Instrument: Comparisons and limitations. *J. Geophys. Res.* **2007**, *112*. [[CrossRef](#)]
17. United States Environmental Protection Agency. What is Acid Rain? Available online: <https://www.epa.gov/acidrain/what-acid-rain> (accessed on 30 July 2017).
18. World Health Organization (WHO). WHO Air Quality Guidelines for Particulate Matter, Ozone, Nitrogen Dioxide and Sulfur Dioxide. Global Update 2005. Available online: [http://apps.who.int/iris/bitstream/10665/69477/1/WHO\\_SDE\\_PHE\\_OEH\\_06.02\\_eng.pdf](http://apps.who.int/iris/bitstream/10665/69477/1/WHO_SDE_PHE_OEH_06.02_eng.pdf) (accessed on 29 June 2017).
19. Levelt, P.F.; van den Oord, G.H.J.; Dobber, M.R.; Mälkki, A.; Visser, H.; de Vries, J.; Stammes, P.; Lundell, J.O.V.; Saari, H. The Ozone Monitoring Instrument. *IEEE Trans. Geosci. Remote Sens.* **2006**, *44*, 1093–1101. [[CrossRef](#)]
20. Corbett, J.J.; Koehler, H.W. Updated emissions from ocean shipping. *J. Geophys. Res.* **2003**, *108*, 4650. [[CrossRef](#)]
21. Endresen, Ø.; Sørgård, E.; Behrens, H.L.; Brett, P.O.; Isaksen, I.S.A. A historical reconstruction of ships' fuel consumption and emissions. *J. Geophys. Res.* **2007**, *112*, D12301. [[CrossRef](#)]
22. Beirle, S.; Boersma, K.F.; Platt, U.; Lawrence, M.G.; Wagner, T. Megacity Emissions and Lifetime of Nitrogen Oxides Probed from Space. *Science* **2011**, *333*, 1737–1739. [[CrossRef](#)] [[PubMed](#)]
23. Janssens-Maenhout, G.; Crippa, M.; Guizzardi, D.; Dentener, F.; Muntean, M.; Pouliot, G.; Keating, T.; Zhang, Q.; Kurokawa, J.; Wankmüller, R.; et al. HTAP\_v2.2: A mosaic of regional and global emission grid maps for 2008 and 2010 to study hemispheric transport of air pollution. *Atmos. Chem. Phys.* **2015**, *15*, 11411–11432. [[CrossRef](#)]
24. Fioletov, V.E.; McLinden, C.A.; Krotkov, N.; Li, C.; Joiner, J.; Theys, N.; Carn, S.; Moran, M.D. A global catalogue of large SO<sub>2</sub> sources and emissions derived from the Ozone Monitoring Instrument. *Atmos. Chem. Phys.* **2016**, *16*, 11497–11519. [[CrossRef](#)]
25. McLinden, C.A.; Fioletov, V.; Shepard, M.W.; Krotkov, N.; Li, C.; Martin, R.V.; Moran, M.D.; Joiner, J. Space-based detection of missing sulphur dioxide sources of global air pollution. *Nat. Geosci.* **2016**, *9*, 496–500. [[CrossRef](#)]
26. Schneider, P.; Lahoz, W.A.; van der A., R. Recent satellite-based trends of tropospheric nitrogen dioxide over large urban agglomerations worldwide. *Atmos. Chem. Phys.* **2015**, *15*, 1205–1220. [[CrossRef](#)]
27. OMSO2 README File v1.1.1 Released Feb 26, 2008 Updated: August 18, 2008. Available online: [https://acdisc.gesdisc.eosdis.nasa.gov/data/s4pa/Aura\\_OMI\\_Level2G/OMSO2G.003/doc/OMSO2G\\_OSIPS\\_README\\_V003.pdf](https://acdisc.gesdisc.eosdis.nasa.gov/data/s4pa/Aura_OMI_Level2G/OMSO2G.003/doc/OMSO2G_OSIPS_README_V003.pdf) (accessed on 17 March 2017).
28. Schoberl, M.R.; Douglass, A.R.; Hilsenrath, E.; Bhartia, P.K.; Beer, R.; Waters, J.W.; Gunson, M.R.; Froidevaux, L.; Gille, J.C.; Barnett, J.J.; et al. Overview of the EOS Aura Mission. *IEEE Trans. Geosci. Remote Sens.* **2006**, *44*, 1066–1074. [[CrossRef](#)]
29. Krotkov, N.A.; Lamsal, L.N.; Celarier, E.A.; Swartz, W.H.; Marchenko, S.V.; Bucsela, E.J.; Chan, K.L.; Wenig, M. The version 3 OMI NO<sub>2</sub> standard product. *Atmos. Meas. Tech. Discuss.* **2017**. [[CrossRef](#)]
30. The OMI Nitrogen Dioxide Algorithm Team. OMNO2 README Document Data Product Version 3.0. Document Version 7.0, September 2016. Available online: [https://acdisc.gesdisc.eosdis.nasa.gov/data/Aura\\_OMI\\_Level2G/OMNO2G.003/doc/README.OMNO2.pdf](https://acdisc.gesdisc.eosdis.nasa.gov/data/Aura_OMI_Level2G/OMNO2G.003/doc/README.OMNO2.pdf) (accessed on 17 March 2017).
31. Seinfeld, J.H.; Pandis, S.N. Chapter 2: Atmospheric Trace Constituents. In *Atmospheric Chemistry and Physics: From Air Pollution to Climate Change*; John Wiley & Sons: Hoboken, NJ, USA, 2016; pp. 45–46.

32. McElroy, M.B.; Salawitch, R.J.; Wofsy, S.C.; Logan, J.A. Reductions of Antarctic ozone due to synergistic interactions of chlorine and bromine. *Nature* **1986**, *321*, 759–762. [[CrossRef](#)]
33. Bowman, K.P. Global Trends in Total Ozone. *Science* **1988**, *239*, 48–50. [[CrossRef](#)] [[PubMed](#)]
34. Pyle, J.A. Stratospheric chemistry and composition, Overview. In *Encyclopedia of Atmospheric Sciences*; Holton, J.R., Curry, J.A., Pyle, J.A., Eds.; Academic Press: London, UK, 2003; Volume 5, pp. 2150–2154.
35. Douglass, A.R.; Newman, P.A.; Solomon, S. The Antarctic ozone hole: An update. *Phys. Today* **2014**, *67*, 42–48. [[CrossRef](#)]
36. Krotkov, N.A.; Li, C.; Leonard, P. *OMI/Aura Sulphur Dioxide (SO<sub>2</sub>) Total Column Daily L2 Global Gridded 0.125 Degree x 0.125 Degree V3*; Goddard Earth Sciences Data and Information Services Center (GES DISC): Greenbelt, MD, USA, 2014.
37. Krotkov, N.A.; Carn, S.A.; Krueger, A.J.; Bhartia, P.K.; Yang, K. Band Residual Difference Algorithm for Retrieval of SO<sub>2</sub> From the Aura Ozone Monitoring Instrument (OMI). *IEEE Trans. Geosci. Remote Sens.* **2006**, *44*, 1259–1266. [[CrossRef](#)]
38. TOMS Science Team. TOMS Nimbus-7 Total Column Ozone Daily L3 Global 1 deg x 1.25 deg Lat/Lon Grid V008, Greenbelt, MD, Goddard Earth Sciences Data and Information Services Center (GES DISC). Available online: [http://disc.sci.gsfc.nasa.gov/datacollection/TOMSN7L3dtoz\\_008.html](http://disc.sci.gsfc.nasa.gov/datacollection/TOMSN7L3dtoz_008.html) (accessed on 16 March 2017).
39. TOMS Science Team. TOMS Nimbus-7 UV Reflectivity Daily L3 Global 1 deg x 1.25 deg Lat/Lon Grid V008, Greenbelt, MD, Goddard Earth Sciences Data and Information Services Center (GES DISC). Available online: [http://disc.sci.gsfc.nasa.gov/datacollection/TOMSN7L3dref\\_008.html](http://disc.sci.gsfc.nasa.gov/datacollection/TOMSN7L3dref_008.html) (accessed on 16 March 2017).
40. Pavón-Carrasco, F.J.; De Santis, A. The South Atlantic Anomaly: The Key for a Possible Geomagnetic Reversal. *Front. Earth Sci.* **2016**. [[CrossRef](#)]
41. Dobber, M.R.; Dirksen, R.J.; Levelt, P.F.; van den Oord, G.H.J.; Voors, R.H.M.; Kleipool, Q.; Jaross, G.; Kowalewski, M.; Hilsenrath, E.; Leppelmeier, G.W.; et al. Rozemeijer. Ozone Monitoring Instrument Calibration. *IEEE Trans. Geosci. Remote Sens.* **2006**, *44*, 1209–1238. [[CrossRef](#)]
42. Ropelewski, C.F.; Jones, P.D. An Extension of the Tahiti-Darwin Southern Oscillation Index. *Mon. Weather Rev.* **1987**, *115*, 2161–2165. [[CrossRef](#)]
43. Gutman, G.; Ignatov, A. Global land monitoring from AVHRR: Potential and limitations. *Int. J. Remote Sens.* **1995**, *16*, 2301–2309. [[CrossRef](#)]
44. Grumm, R.H.; Hart, R. Standardized Anomalies Applied to Significant Cold Season Weather Events: Preliminary Findings. *Weather Forecast.* **2001**, *16*, 736–754. [[CrossRef](#)]
45. Hartmann, D.L.; Klein Tank, A.M.G.; Rusticucci, M.; Alexander, L.V.; Brönnimann, S.; Charabi, Y.; Dentener, F.J.; Dlugokencky, E.J.; Easterling, D.R.; Kaplan, A.; et al. Observations: Atmosphere and Surface. In *Climate Change 2013: The Physical Science Basis. Contribution of Working Group I to the Fifth Assessment Report of the Intergovernmental Panel on Climate Change*; Stocker, T.F., Qin, D., Plattner, G.-K., Tignor, M., Allen, S.K., Boschung, J., Nauels, A., Xia, Y., Bex, V., Midgley, P.M., Eds.; Cambridge University Press: New York, NY, USA, 2013; pp. 159–254.
46. Salmi, T.; Määttä, A.; Anttila, P.; Ruoho-Airola, T.; Amnell, T. *Detecting Trends of Annual Values of Atmospheric Pollutants by the Mann-Kendall Test and Sen's Slope Estimates-The Excel Template Application Makesens*; Publications on air quality, volume 31; Finish Meteorological Institute: Helsinki, Finland, 2002.
47. Thousands Flee as Volcano Erupts in Congo. Daily Mail, 18 January 2002. Available online: <http://www.dailymail.co.uk/news/article-95518/Thousands-flee-volcano-erupts-Congo.html> (accessed on 15 June 2017).
48. Petersen, K. One of Africa's Most Active Volcanoes Is Showing New Signs of Life. Public Radio International, 2 May 2016. Available online: <https://www.pri.org/stories/2016--05--02/one-africas-most-active-volcanos-showing-new-signs-life> (accessed on 16 June 2017).
49. Oppenheimer, C. Satellite Observations of Lava Lake Activity at Nyiragongo Volcano, Ex-Zaire, during the Rwandan Refugee Crisis. *Disasters* **1998**, *22*, 268–281. [[CrossRef](#)] [[PubMed](#)]
50. Carn, S.A.; Fioletov, V.E.; McLinden, C.A.; Li, C.; Krotkov, N.A. A decade of global volcanic SO<sub>2</sub> emissions measured from space. *Sci. Rep.* **2017**, *7*, 44095. [[CrossRef](#)]
51. Core Writing Team. *Climate Change 2014: Synthesis Report. Contribution of Working Groups I, II and III to the Fifth Assessment Report of the Intergovernmental Panel on Climate Change*; Pachauri, R.K., Meyer, L.A., Eds.; IPCC: Geneva, Switzerland, 2014.

52. Rutllant, J.; Garreaud, R. Meteorological air pollution potential for Santiago, Chile: Towards an objective episode forecasting. *Environ. Monit. Assess.* **1995**, *34*, 223–244. [[CrossRef](#)] [[PubMed](#)]
53. Romero, H.; Ihl, M.; Rivera, A.; Zalazar, P.; Azocar, P. Rapid urban growth, land-use changes and air pollution in Santiago, Chile. *Atmos. Environ.* **1999**, *33*, 4039–4047. [[CrossRef](#)]
54. Kirchhoff, V.W.J.H.; Setzer, A.W.; Pereira, M.C. Biomass burning in Amazonia: Seasonal effects on atmospheric O<sub>3</sub> and CO. *Geophys. Res. Lett.* **1989**, *16*, 469–472. [[CrossRef](#)]
55. Duncan, B.N.; Martin, R.V.; Staudt, A.C.; Yevich, R.; Logan, J.A. Interannual and seasonal variability of biomass burning emissions constrained by satellite observations. *J. Geophys. Res.* **2003**, *108*, 4100. [[CrossRef](#)]
56. Xiao, Z.; Jiang, H.; Song, X.; Zhang, X. Monitoring of atmospheric nitrogen dioxide using Ozone Monitoring Instrument remote sensing data. *J. Appl. Remote Sens.* **2013**, *7*. [[CrossRef](#)]
57. Van der A, R.J.; Eskes, H.J.; Boersma, K.F.; van Noije, T.P.C.; Van Roozendael, M.; De Smedt, I.; Peters, D.H.M.U.; Meijer, E.W. Trends, seasonal variability and dominant NO<sub>x</sub> source derived from a ten year record of NO<sub>2</sub> measured from space. *J. Geophys. Res.* **2008**, *113*, D04302. [[CrossRef](#)]
58. Civil Aviation Authority of New Zealand. Ash Cloud from Chilean Volcano Entering New Zealand Airspace. 11 June 2011. Available online: <https://www.caa.govt.nz/publicinfo/med-rel-ash-cloud/> (accessed on 24 July 2017).
59. More Delays Ahead as Ash Cloud Circles. ABC News, 13 June 2011. Available online: <http://www.abc.net.au/news/2011-06-14/more-delays-ahead-as-ash-cloud-circles/2757060> (accessed on 24 July 2017).
60. Calkins, C.; Ge, C.; Wang, J.; Anderson, M.; Yang, K. Effects of meteorological conditions on sulphur dioxide air pollution in the North China plain during winters of 2006–2015. *Atmos. Environ.* **2016**, *147*. [[CrossRef](#)]
61. Qu, Z.; Henze, D.K.; Capps, S.L.; Wang, Y.; Xu, X.; Wang, J.; Keller, M. Monthly top-down NO<sub>x</sub> emissions for China (2005–2012): A hybrid inversion method and trend analysis. *J. Geophys. Res.* **2017**, *122*, 4600–4625. [[CrossRef](#)]
62. Nguyen, H.; Evans, A.; Lucas, C.; Smith, I.; Timbal, B. The Hadley Circulation in Reanalyses: Climatology, Variability, and Change. *J. Clim.* **2013**, *26*, 3357–3376. [[CrossRef](#)]
63. Vallis, G.K. The Overturning Circulation: Hadley and Ferrel Cells. In *Atmospheric and Oceanic Fluid Dynamics: Fundamentals and Large-Scale Circulation*; Cambridge University Press: Cambridge, UK, 2006; pp. 451–484.
64. Allen, R.J.; Norris, J.R.; Kovilakam, M. Influence of anthropogenic aerosols and the Pacific Decadal Oscillation on tropical belt width. *Nat. Geosci.* **2014**, *7*, 270–274. [[CrossRef](#)]
65. Polvani, L.M.; Waugh, D.W.; Correa, G.J.P.; Son, S.-W. Stratospheric Ozone Depletion: The Main Driver of Twentieth-Century Atmospheric Circulation Changes in the Southern Hemisphere. *J. Clim.* **2011**, *24*, 795–812. [[CrossRef](#)]
66. Garfinkel, C.I.; Waugh, D.W.; Polvani, L.M. Recent Hadley cell expansion: The role of internal atmospheric variability in reconciling modelled and observed trends. *Geophys. Res. Lett.* **2015**, *42*, 10824–10831. [[CrossRef](#)]
67. Hoskins, B.J.; Hodges, K.I. A New Perspective on Southern Hemisphere Storm Tracks. *J. Clim.* **2005**, *20*, 4108–4129. [[CrossRef](#)]
68. Archer, C.L.; Caldeira, K. Historical trends in the jet streams. *Geophys. Res. Lett.* **2008**, *35*, L08803. [[CrossRef](#)]
69. Calvert, J.G.; Su, F.; Bottenheim, J.W.; Strausz, O.P. Mechanism of the homogeneous oxidation of sulfur dioxide in the troposphere. *Atmos. Environ.* **1978**, *12*, 197–226. [[CrossRef](#)]
70. Clemitshaw, K.C.; Weiss-Penzias, P.S. Tropospheric chemistry and composition: Hydroxyl Radical. In *Encyclopedia of Atmospheric Sciences*; Holton, J.R., Curry, J.A., Pyle, J.A., Eds.; Academic Press: London, UK, 2003; Volume 6, pp. 2403–2411.
71. Hegg, D.A.; Hobbs, P.V. Oxidation of sulphur dioxide in aqueous systems with particular reference to the atmosphere. *Atmos. Environ.* **1978**, *12*, 241–253. [[CrossRef](#)]
72. Berresheim, H.; Andreae, M.O.; Ayers, G.P.; Gillett, R.W.; Merrill, J.T.; Davis, V.J.; Chameides, W.L. Airborne measurements of dimethylsulfide, sulfur dioxide, and aerosol ions over the Southern Ocean South of Australia. *J. Atmos. Chem.* **1990**, *10*, 341–370. [[CrossRef](#)]
73. Ehhalt, D.H.; Wahner, A. Tropospheric chemistry and composition: Oxidizing Capacity. In *Encyclopedia of Atmospheric Sciences*; Holton, J.R., Curry, J.A., Pyle, J.A., Eds.; Academic Press: London, UK, 2003; Volume 6, pp. 2415–2424.

74. Duncan, B.N.; Lamsal, L.N.; Thompson, A.M.; Yoshida, Y.; Lu, Z.; Streets, D.G.; Hurwitz, M.M.; Pickering, K.E. A space-based, high-resolution view of notable changes in urban NO<sub>x</sub> pollution around the world (2005–2014). *J. Geophys. Res.* **2016**, *121*, 976–996. [[CrossRef](#)]
75. Smith, S.J.; van Aardenne, J.; Klimont, Z.; Andres, R.J.; Volke, A.; Delgado Arias, S. Anthropogenic sulfur dioxide emissions: 1850–2005. *Atmos. Chem. Phys.* **2011**, *11*, 1101–1116. [[CrossRef](#)]



© 2017 by the authors. Licensee MDPI, Basel, Switzerland. This article is an open access article distributed under the terms and conditions of the Creative Commons Attribution (CC BY) license (<http://creativecommons.org/licenses/by/4.0/>).